Structural basis of CHMP2A-CHMP3 ESCRT-III polymer assembly and membrane cleavage

Kimi Azad, Delphine Guilligay, Cécile Boscheron, Sourav Maity, Nicola de Franceschi, Guidenn Sulbaran, Grégory Effantin, Haiyang Wang, Jp Kleman, Patricia Bassereau, et al.

Structural basis of CHMP2A-CHMP3 ESCRT-III polymer assembly and membrane cleavage

Kimi Azad[1], Delphine Guilligay[1], Cecile Boscheron[1,4], Sourav Maity[2,4], Nicola De Franceschi[1,3,4], Guidenn Sulbaran[1], Gregory Effantin[1], Haiyan Wang[1], Jean-Philippe Kleman[1], Patricia Bassereau[3], Guy Schoehn[1], Wouter H Roos[2], Ambroise Desfosses[1,*], Winfried Weissenhorn[1,*]

[1] Univ. Grenoble Alpes, CEA, CNRS, Institut de Biologie Structurale (IBS), Grenoble, France.
[2] Moleculaire Biofysica, Zernike Instituut, Rijksuniversiteit Groningen, Groningen, Netherlands.
[3] Institut Curie, Université PSL, Sorbonne Université, CNRS, Laboratoire Physico Chimie Curie, Paris, France.
[4] These authors contributed equally

*Correspondence: ambroise.desfosses@ibs.fr and winfried.weissenhorn@ibs.fr

Abstract

The endosomal sorting complex required for transport (ESCRT) is a highly conserved protein machinery that drives a divers set of physiological and pathological membrane remodeling processes. However, the structural basis of ESCRT-III polymers stabilizing, constricting and cleaving negatively curved membranes is yet unknown. Here we present cryo electron microscopy structures of membrane-coated CHMP2A-CHMP3 filaments of two different diameters at 3.3 and 3.6 Å resolution. The structures reveal helical filaments assembled by CHMP2A-CHMP3 heterodimers in the open ESCRT-III conformation, which generates a partially positive charged membrane interaction surface, positions short N-terminal motifs for membrane interaction and the C-terminal VPS4 target sequence towards the tube interior. Inter-filament interactions are electrostatic, which may facilitate filament sliding upon VPS4-mediated polymer remodeling. Fluorescence microscopy as well as high speed atomic force microscopy imaging corroborate that CHMP2A-CHMP3 polymers and VPS4 can constrict and cleave narrow membrane tubes, thus acting as a minimal membrane fission machinery.

Introduction

The endosomal sorting complex required for transport (ESCRT) machinery catalyzes many divergent membrane remodeling processes including the formation of multivesicular endosomes, cytokinesis, nuclear envelope reformation, membrane repair, autophagy, exosome biogenesis, neuronal pruning, dendritic spine maintenance, enveloped virus budding, release of peroxisomes and of recycling endosomes [1-9].

Common to all ESCRT-catalyzed processes in eukaryotes, archaea and bacteria is the recruitment of ESCRT-III proteins that polymerize to generate and/or to stabilize membranes with either flat, negatively or positively curved geometries [10-16]. The principal function of the polymers is to induce membrane constriction via outside-in fission of tubular structures with ESCRT-III protein coats on the outside of a membrane tube or inside-out fission with ESCRT-III polymers assembled within membrane neck/tube structures formed during vesicle and virus budding or at the cytokinetic midbody [10,13,16-19].

Humans express eight ESCRT-III proteins that can comprise several isoforms per member, corresponding to eight homologues in *S. cerevisiae* (in parentheses) named CHMP1A/B (Did2), CHMP2A/B (Vps2), CHMP3 (Vps24), CHMP4A/B/C (Snf7), CHMP5 (Vps60), CHMP6 (Vps20), CHMP7 (CHM7) and CHMP8/IST1 (Ist1) [10]. *S. cerevisiae* assembles two ESCRT-III subcomplexes, Vps20/Snf7 that in turn recruits Vps24/Vps2 [20] consistent with CHMP4 recruiting

CHMP3 and CHMP2A [21]. Notably, Vps24 (CHMP3) and Vps2 (CHMP2) have been suggested to block Snf7 (CHMP4) polymerization and cap ESCRT-III assembly prior to recycling [22,23]. Consistent with the idea of a core ESCRT-III, HIV-1 budding can be catalyzed with a minimal set of one CHMP4 and one CHMP2 isoform [21]. Although CHMP3 is not strictly required, truncated versions thereof exert a potent dominant negative effect on HIV-1 budding [24,25] and CHMP3 synergizes HIV-1 budding efficiency with CHMP2A but not with CHMP2B [26]. Thus ESCRT-III CHMP4, CHMP2 and CHMP3 constitute a minimal machinery that together with VPS4 catalyzes membrane fission from within membrane necks as proposed by *in vitro* reconstitution [27].

ESCRT-III proteins adopt a closed conformation in the cytosol [28-30]. Membrane recruitment via ESCRT-I, ESCRT-II or Alix/Bro1 [31-34] is thought to induce ESCRT-III activation, which entails opening of the closed conformation [24,35,36] to an extended open polymerization-competent conformation as first shown for CHMP1B [37]. The CHMP1B polymer stabilizes positively curved membranes and can co-polymerize with IST1 in the closed conformation thereby forming an outer layer on top of the inner open conformation CHMP1B layer [37], whose interplay leads to membrane tube thinning and cleavage [17,38].

CHMP4 homologues, Snf7 and shrub, adopt similar open conformations within crystalline polymers [39,40]. Notably *in vitro* CHMP4 polymers interact with flat membranes, [41-43] and stabilize positively curved membranes in the presence of CHMP2A (Vps2) and CHMP3 (Vps24) [11,12]. Furthermore, CHMP4 was proposed to interact with negatively curved membranes [44] and CHMP4 spirals have been imaged within membrane tubes *in vivo* [45,46] leading to the model of ESCRT-III spiral springs assembling on flat membranes driving membrane deformation [42].

The conservation of the structural principle of the open ESCRT-III conformation is further underlined by the structures of plastid and bacterial membrane repair proteins Vipp1 and PspA, which both stabilize positively curved membranes and corroborate the conservation of the ESCRT-III machinery throughout all kingdoms of life [14,15,47].

While these structures demonstrate filament formation to stabilize positively curved membranes only low resolution models of filaments stabilizing negatively curved membranes have yet been imaged revealing single and multi-stranded polymers *in vitro* [11,12,29,41-43,48-51] and *in vivo* [43,45,46,52-55]. Consistent with their central role in membrane fission catalyzed from within membrane necks, ESCRT-III CHMP2A and CHMP3 form helical tubular structures with defined diameters *in vitro,* which have been suggested to stabilize negative membrane curvature [26,48]. VPS4 constricts these filaments producing dome-like end caps prior to complete polymer disassembly *in vitro* [56] in agreement with the proposal of VPS4-driven subunit extraction and filament closure [57] and

continuous ESCRT-III turn-over *in vivo* [43,58,59]. Notably, *S. cerevisiae* Vps2 and Vps24 form similar helical tubes that, however, seem to require Snf7 for polymerization [51].

Because most ESCRT-catalyzed processes act on negatively curved membranes to catalyze inside-out membrane fission, we set out to determine the structural basis of ESCRT-III stabilizing negatively curved membranes. We reconstituted CHMP2A-CHMP3 polymers within membrane tubes, solved their structure by cryo electron microscopy and show that VPS4 can indeed constrict CHMP2A-CHMP3 membrane tubes to the point of fission, corroborating that CHMP2A and CHMP3 form a minimal membrane fission complex powered by VPS4 and ATP.

Results

Structure of the CHMP2A-CHMP3 polymer assembled within membrane tubes

CHMP3 full length (residues 1-222) and C-terminally truncated CHMP2A (residues 1-161) were assembled into helical tubular structures as described [48]. After removal of the N-terminal tags, the tubular structures were coated with lipid bilayer, which tightly associated with the protein layer as shown by cryo electron microscopy (cryo-EM) **(Extended Data Fig.1a**). 2D classification of the manually picked tube-like structures generated a dataset composed of 5 different diameters ranging from 380 Å to 490 Å, with the 410 Å (51.4%) and 430 Å (31.2%) diameters representing the most populated classes (**Extended Data Fig.1b**). The power spectra of the segments of the class averages of the two diameters (**Extended Data Fig.1c and d**) were then employed to explore possible helical symmetries and combined with helical real-space reconstruction [60] to validate the symmetry parameters. This revealed that the 410 Å and 430 Å diameter tubes are formed by elementary helices composed of respectively 6.3 and 6.6 units per turn with a small pitch of 9 Å for the 410 Å diameter and 18 Å for the 430 Å diameter. The latter displays an additional C2 symmetry around the helical axis, explaining the doubling of the pitch (**Extended Data Fig.1c and d**). Although, the asymmetric units along the elementary helix are not biochemically connected, they translate into filaments with extended interaction surfaces between subsequent asymmetric units. The symmetry parameters of the filaments are relatively similar for both diameters (Rise/Twist of 8.227 Å /16.877° and 8.641 Å /17.701° for the 410 Å and 430 Å diameters, respectively), and therefore likely represent the preferred polymerization mode of the repeating unit, the CHMP2A-CHMP3 heterodimers (**Extended Data Fig.1c and d**).

Six filaments (2*3 in the case of the C2 symmetric helix) form left-handed six-start helices with helical pitches of ~175 Å for both diameters (**Fig. 1a and b**). The 430 Å filament is composed of 21.33 units per turn (**Fig. 1a and b**) and the 410 Å filament contains 20.33 units per turn (**Fig. 1c and d**), indicating a helical repeat after three turns and similar inter-filament interactions along

the helical axis. Comparison of the 430 and 410 Å diameter tubes demonstrates that removal of one heterodimer reduces the tube diameter by 20 Å.

The three-dimensional (3D) helical reconstruction shows an overall resolution of 3.6 Å for the 410 Å and 3.3 Å for the 430 Å diameter (**Fig. 1; Extended Data Fig.2 and 3a**) with local resolutions ranging from 3.3 Å to 4.6 Å for the 430 Å diameter and 3.6 to 5.2 Å for the 410 Å diameter (**Extended Data Fig.3b and c).** The map of the 430 Å diameter (**Fig. 1e**) was employed to build the atomic model of the repeating unit of the filament, formed by the CHMP2A-CHMP3 heterodimer revealing both protomers in the open ESCRT-III conformation (**Fig. 1f and Extended Data Fig.3d, Table 1**).

Comparison of the closed [28,29] and open CHMP3 conformations showed the conformational transitions upon CHMP3 activation, which involves extension of the helical hairpin (residues P12-A101) that is identical in both conformations (r.m.s.d. of 1.082 Å) by a linker and helix 3 (L117). The following short connection forms an elbow and translates helix 4 by ~10 Å positioning helix 4 in a 140° angle with respect to the hairpin axis. Helix 4 is composed of the closed conformation helix 4 and most of the disordered linker connecting to helix 5 via a 90° kink at positions M151 to D152 (**Fig. 2a**). The remaining CHMP3 residues 170 to 220 are flexible and disordered in the structure. Both CHMP3 and CHMP2A open conformations are similar as superposition of their Cα atoms revealed an r.m.s.d. of 0.934 Å (**Fig.3a**), suggesting that CHMP2A can fold into the same closed conformation structure as CHMP3.

The repeating unit of the filament is the CHMP2A-CHMP3 heterodimer formed by parallel interaction of their hairpins with the CHMP2A hairpin tip shifted by six helical turns with respect to CHMP3 (**Fig. 2b**). The heterodimer interaction covers 2026 $Å^2$ of CHMP2A and 1997 $Å^2$ of CHMP3 surfaces involving 55 and 51 interface residues, respectively. The structure of the heterodimer was further confirmed by mutagenesis. Introducing pairs of cysteine demonstrated that CHMP2A_D57C together with CHMP3_S75C and CHMP2A_N18C together with CHMP3_V110C (**Extended Data Fig.4a**) assembled into disulfide-linked heterodimers upon polymerization into tube-like structures as shown by SDS-PAGE analyses and negative staining EM (**Extended Data Fig.4b and b**). Furthermore, mutagenesis of CHMP2A-CHMP3 interface residues (**Extended Data Fig.4d**) prevented polymerization as expected (**Extended Data Fig.4e**). The principle of the heterodimer hairpin stacking is employed to assemble the filament, which is further stabilized by lateral interactions of CHMP3i elbow helix 4 with CHMP2Ai, CHMP3i^{+1} and CHMP2Ai^{+1}. In addition, CHMP3i helix 5 interacts with the tip of the CHMP3i^{+2} hairpin (**Fig. 2b**), as observed in the closed conformation (**Fig. 2a**) [28,29]. Similar to CHMP3, CHMP2A helix 4 exerts the same domain exchange interactions (**Fig. 2b**). Cα superposition of the open CHMP3 conformation

revealed the closest match with the *S. cerevisiae* Snf7 protomer up to helix 4 (**Fig.3b**) and considerable differences with CHMP1B, Vipp1, PspA and Vps24 [14,15,37,47,61] (**Fig.3c-f**). Notably, different hairpin interactions and orientations of the helical arms upon polymerization determine the filament geometry that leads to positively curved membrane interaction by CHMP1B, Vipp1 and PspA [14,15,37,47] underlining the extensive structural plasticity of ESCRT-III proteins.

CHMP2A-CHMP3 polymer interaction with membrane

The CHMP2A-CHMP3 polymer is tightly associated with the lipid bilayer, which has a width of ~50 Å (**Fig.4a; Extended Data Fig.1e and f**). Comparison of the membrane diameters of CHMP2A-CHMP3 coated tubes with protein-free vesicles generated during the membrane-coating process suggests thinning of the membrane upon interaction with the polymer, because protein-free vesicles revealed diameters of ~58 Å (**Extended Data Fig.1g and h**). Both CHMP2A and CHMP3 expose the same regions to the membrane including the positioning of their N-terminal regions at the membrane interface. Although CHMP3 residues 1-10 and CHMP2A residues 1- 7 are disordered, they are both oriented towards the lipid bilayer by conserved proline residues (**Fig. 4a and Extended Data Fig.5a**) consistent with previous suggestions that short amphipathic N-terminal helices insert into the bilayer [52,62]. The main membrane interaction surfaces locate to the elbow formed by helices 3 and 4 (residues K104 to R131) exposing six basic residues of CHMP2A (K104, K108, R115, K118, K124, R131) and five basic residues of CHMP3 (K106, K112, K119, K132, K136) prone to interact with negative charges of the membrane (**Fig. 4b**). The electrostatic potential map shows in addition to the stretch of basic surfaces some negative and non-charged regions on the outer polymer surface (**Fig. 4c**). Most of the basic residues are conserved in *S. cerevisiae* Vps2 and Vps24 (**Extended Data Fig.5a**). Notably, alanine mutagenesis of some CHMP3 basic residues within the membrane interaction surface did not interfere with CHMP2A-CHMP3 polymerization *in vitro* (**Extended Data Fig.6a)** nor did they affect the dominant negative effect of C-terminally truncated CHMP3 on HIV-1 Gag VLP release (**Extended Data Fig.7b**), indicating that membrane binding is complex and not only electrostatic, consistent with plasma membrane localization of the CHMP3 mutant (**Extended Data Fig.7c**).

Inter-filament interactions

Conserved basic helix 1 residues of CHMP2A and CHMP3 (**Extended Data Fig.5a**) are at the filament interface opposed by a stretch of conserved acidic residues within helices 4 and 5 (**Extended Data Fig.5a**) of neighboring filaments (**Fig. 4d**), which indicate electrostatic inter-filament interactions (**Fig. 4c**). Mutation of the helix 1 basic cluster within either CHMP2A or

CHMP3 prevented polymer formation *in vitro* (**Extended Data Fig.6d**), indicating that the basic charge of helix 1 is important for filament polymerization, which is in line with mutagenesis of a similar cluster of basic residues within helix 1 of CHMP3 abolishing its dominant negative effect on HIV-1 budding [28]. To further test the electrostatic inter-filament interactions, we exposed the helical tubular CHMP2A-CHMP3 polymers to high ionic strength. This led to the partial unwinding of the filaments producing single and multi-stranded filaments (**Extended Data Fig.7a-e**) in agreement with the presence of single and multi-start helices upon CHMP2A-CHMP3 polymerization *in vitro* [26]. We suggest that these electrostatic interactions between filaments enable filament sliding upon VPS4-catalyzed remodeling. The acidic cluster in helices 4 and 5 is conserved in CHMP4A, B, C, CHMP5 and CHMP6 (**Extended Data Fig.5b**) indicating potential similar involvement in inter-filament interaction for the formation of mixed filaments. Notably, the acidic cluster is not conserved in CHMP1A and B, which stabilizes positively curved membranes via basic charges present on the inside of the protein tube-like polymer [37]. We therefore suggest that the acidic cluster is a hallmark of ESCRT-III stabilizing negatively curved membrane structures.

VPS4 remodels and cleaves CHMP2A-CHMP3 membrane tubes

We next tested whether VPS4B can remodel the CHMP2A-CHMP3 membrane coated tubes as we have shown before for CHMP2A-CHMP3 tubes without membrane [48,56]. When we incubated CHMP2A-CHMP3 and VPS4B containing membrane tubes (**Extended Data Fig.8a**) with ATP and Mg^{2+}, complete disassembly of the tubes can be occasionally observed (**Extended Data Fig.8b and c**). In order to image tube remodeling by fluorescence microscopy, VPS4B and caged ATP were incorporated into the tubes wrapped with fluorescently labelled membrane. Imaging of tubes containing either only caged ATP (**Fig. 5a and b**; **movie 1; Extended Data Fig.9a and b; movie 2)** or only VPS4B (**Fig. 5c and d; movie 3**) demonstrated that photolysis used to uncage ATP did not affect the tube structure. However, tubes containing both caged ATP and VPS4B revealed constriction and tube cleavage upon ATP activation at different sites starting at 30s leading to complete disassembly within 270s (**Fig. 5e and f; movie 4**) or starting at 69s (**Extended Data Fig.9c and d; movie 5**) or at 50 s (**movie 6**).

Tube cleavage was further confirmed by high-speed AFM (HS-AFM) imaging. First, CHMP2A-CHMP3 tubes with and without membrane were imaged (**Extended Data Fig.10a-c**). A comparative height histogram showed an increase in tube height of ~8 nm for the membrane coated tubes (**Extended Data Fig.10d**), as expected for unilamellar membrane coating. Next, membrane-coated tubes loaded with 10 mM caged ATP with and without UV exposure (**Extended**

Data Fig.10e; movie 7) were recorded by HS-AFM. In the absence of VPS4B, photolysis of the caged ATP did not induce changes in tube morphology, consistent with the observations by fluorescence microscopy. Further, no changes in tube morphology were observed without UV exposure for an extended period of time of CHMP2A-CHMP3 tubes coated with membrane and loaded with VPS4B and caged ATP **(Fig. 6a, movie 8)**. However, upon UV exposure, constriction and cleavage of the membrane coated tubes was observed (**Fig. 6b; movie 9**). Kymographs along the tube cross section (**Fig. 6c**) and the evolution of the height at the constriction sites over time (**Fig. 6d**) reveal that complete cleavage of the membrane tube occurs within a time period of ~ 200 s of UV exposure. We conclude that VPS4B can constrict the CHMP2A-CHMP3 filaments bound to membranes that leads to membrane cleavage, reminiscent of membrane fission.

Discussion

The structure of the CHMP2A-CHMP3 heteropolymer demonstrates how ESCRT-III filaments polymerize into rigid structures that can stabilize and/or shape negatively curved membrane necks with diameters of approximately 50 nm. Such membrane structures are present at many ESCRT-catalyzed processes including vesicle and virus budding or at later stages during cytokinetic midbody constriction [10,63]. Although the structural principles of the open ESCRT-III conformation are highly conserved between CHMP2A/CHMP3 and CHMP1B [37], Snf7/Shrub (CHMP4) [39,40] and bacterial PspA and Vipp1 [14,15,47], differences in helical hairpin stacking and orientations of the helical arms dictates the geometry of the filaments that stabilize positively curved membrane or negatively curved membrane as in case of CHMP2A-CHMP3 polymerization. Furthermore, assembly modes of ESCRT-III monomers can vary as shown for CHMP2A, CHMP3 and CHMP4B, which can yet adapt another filament geometry that stabilizes positively curved membranes [11,12]. Thus the plastic nature of ESCRT-III protein conformations can lead to variable ESCRT-III filament geometries that can adapt a wide range of curvatures to accommodate ESCRT function in different membrane remodeling processes [16].

A striking feature of the CHMP2A-CHMP3 polymer is the narrow range of tube diameters, indicative of a late recruitment during the constriction process. During yeast MVB biogenesis, Vps24/Vps2 (CHMP3/CHMP2) is indeed recruited last prior to complete ESCRT-III disassembly and probably completion of fission [20,22,23]. Likewise, CHMP4 isoforms recruit CHMP3 and CHMP2A to HIV-1 budding sites [21,64,65]. The narrow range of diameters of the CHMP2A-CHMP3 polymer structure suggests that recruitment of CHMP3 and CHMP2A molds membrane necks into approximately 40 to 50 nm diameters, which sets the stage for further constriction. Comparison of the 410 and 430 Å wide structures shows that removal of only one CHMP2A-CHMP3 heterodimer

per filament turn reduces the tube diameter by 20 Å, indicating how a stepwise removal of heterodimers can successively induce membrane constriction.

Another feature of the tubular polymer is that it can assemble from single or multi-stranded filaments [26] the latter being the preferred assembly *in vitro*. Interaction between filaments is driven by complementary positive and negative charges. However, surprisingly, high ionic strength did not disassemble the tube consistently into individual filaments but partially preserved the multi-strand architecture *in vitro*. The 17.5 nm width of the six-stranded helix present in the structure fits the 17 nm wide helices imaged at the midbody [53], suggesting that such spirals contain six ESCRT-III filaments. Since inter-filament interactions are electrostatic, different ESCRT-III filaments may contribute to the formation of mixed multi-stranded filaments [43,66]. In line, acidic residues within helix 4 and basic residues within helix 1 have been implicated in *S. cerevisiae* Snf7-Vps24 interaction [67]. Because basic and acidic charges within these regions are conserved in CHMP6, CHMP4A, B, C, CHMP2B and CHMP5, filaments thereof may also form side by side via homo- or hetero-filament assembly. The loose electrostatic inter-filament interactions likely facilitate sliding of filaments upon ESCRT-III filament remodeling by VPS4, which catalyzes filament constriction prior to complete disassembly [56]. Notably, dynamic VPS4-mediated turnover of ESCRT-III has been proposed in different membrane remodeling processes [43,58,59].

CHMP2A-CHMP3 polymers have been suggested to interact with negatively charged membranes [68-70], which is confirmed by the cluster of basic residues within the membrane interaction surface. Furthermore, the structure indicates that short N-terminal hydrophobic motifs, implicated in ESCRT-III function [52 62] are positioned to insert into the membrane. Although this N-terminal motif is helical in a filament structure assembled by an intermediate Vps24 (CHMP3) conformation [61], the corresponding helices of CHMP2A and CHMP3 are not visible in the membrane-bound structure suggesting that the putative amphipathic helices can adopt different membrane insertion angles. Polymer interaction with membrane is tight, which likely excludes membrane proteins from the site of polymerization *in vivo* thereby serving as a diffusion barrier [70]. The thickness of the membrane bound to the polymer is ~50 Å as compared to ~58 Å of protein-free vesicles generated during the CHMP2A-CHMP3 membrane-coating process, which indicates that CHMP2A-CHMP3 membrane interaction may induce membrane reorganization leading to membrane thinning as reported for the CHMP1B-IST1 polymers [17].

CHMP3 is dispensable for HIV-1 budding [21] and *S. cerevisiae* Vps24 can be substituted by Vps2 overexpression restoring partial endosomal cargo sorting [71]. Both processes depend on CHMP2A and Vps2 interaction with CHMP4 or Snf7 [22, 21]. The structure suggests that CHMP3 can be structurally replaced by CHMP2A in the polymer, indicating that CHMP2A filaments on their

own may form similar helices. Although CHMP2A can polymerize into circular filaments with approximate diameters of 40 nm that often coil up, no regular CHMP2A tube-like structures have been yet imaged *in vitro* [26].

VPS4B remodels CHMP2A-CHMP3 helical tubular structures *in vitro* [48,72] inducing filament constriction and cleavage that generates dome-like end caps prior to complete disassembly, which was proposed to drive membrane fission [56,73]. Here, we show that VPS4B constricts and cleaves CHMP2A-CHMP3 membrane-coated tubes via membrane fission likely via the formation of dome-like end-caps [56]. Cleavage of membrane tubes pulled from GUVs has been proposed previously by employing a minimal system composed of *S. cerevisiae* Snf7, Vps24, Vps2 and Vps4 [27], while another model suggested sequential recruitment of *S. cerevisiae* Snf7, followed by Vps2-Vps24, Vps2-Did2 and Did2-Ist1 for final constriction [66]. Our data indicate that CHMP2A-CHMP3 filaments constitute together with VPS4 a minimal ESCRT-III membrane fission machinery that can constrict membrane necks with 40 to 50 nm large diameters to the point of fission. It is yet unclear how many helical turns are required for constriction *in vivo*, although more than one, as estimated from imaging [59], would allow filament sliding powered by ATP-driven forces that can drive filament-induced membrane constriction and cleavage. Finally, catalyzing membrane fission with a minimal machinery is well in line with ancestral ESCRT-III function [74,75].

Methods

Expression and purification

CHMP2AΔC containing residues 1 to 161 was subcloned in a pMAL-c5X vector with an additional TEV site at the amino terminal end and expressed as a MBP fusion protein in the C41 (DE3) *E. coli* bacterial strain (Lucigen). Expression was induced for 1h at 37°C. Bacteria were lysed by sonication in a buffer containing 50 mM HEPES pH 7.5, 300 mM NaCl, 1 mM DTT, 5 mM EDTA and protease inhibitors. Cleared lysate was applied onto an amylose resin (New England Biolabs), washed with buffer A (25mM HEPES 7.5, 150 mM NaCl, 1mM DTT), then with Buffer B (25 mM HEPES pH 7.5, 1 M NaCl, 1 M KCl, 1mM DTT) followed by a last wash with Buffer A. Finally, protein was eluted with buffer C (25 mM HEPES 7.5, 150 mM NaCl, 10 mM maltose). The most concentrated fraction was directly applied to size exclusion chromatography (SEC) Superdex 200 column (GE Healthcare) in buffer D (25 mM HEPES pH 7.5, 150 mM NaCl).

Full-length CHMP3 was subcloned in a pProEX-HTb vector (Life Technologies, Thermo Fisher) and expressed in BL21Gold (DE3) *E. coli* bacterial strain (Agilent). Expression was induced for 3h at 37°C and purified as described [48] with minor modifications. Bacteria were lysed by sonication

in buffer E (25 mM HEPES pH 7.5, 150 mM NaCl, 10mM imidazole) containing protease inhibitors and the cleared lysate was applied onto a Ni^{2+}-chelating sepharose (Cytivia), washed extensively with lysis buffer E, and subsequently with buffer F (25 mM HEPES pH 7.5, 300 mM NaCl, 300 mM KCl, 20 mM imidazole) and buffer G (25 mM HEPES pH 7.5, 300 mM NaCl, 300 mM KCl, 50 mM imidazole). Finally, CHMP3 was eluted with buffer H (25 mM HEPES 7.5, 150 mM NaCl, 350 mM imidazole) and cleaved overnight at 4°C with Tobacco Etch Virus (TEV) protease at 1:100 (w/w) ratio in the presence of 10 mM β-mercaptoethanol. Cleaved protein was then applied on a second Ni^{2+}-chelating sepharose in order to remove TEV, the His-tag and uncleaved protein. The final step included size exclusion chromatography (SEC) on a Superdex 75 column (GE Healthcare) in buffer D. CHMP3 concentrated at 300 µM was frozen for further use.

CHMP2AΔC-mutants containing residues 9 to 161 and CHMP3-mutants containing residues 9 to 183 were synthesized (ThermoFisher), subcloned in a pETM40 vector (PEPcore facility-EMBL Heidelberg) and the pProEX-HTb (ThermoFisher) vector, respectively. Mutants were expressed and purified as described above for wild type sequences.

CHMP2A-CHMP3 membrane tube generation

For helical tube formation as described previously [48], 10 µM CHMP2AΔC was mixed with 20 µM full-length CHMP3 and incubated for 48-72h at 4°C. After incubation, tubes were harvested by centrifugation at 20,000g for 30min and the pellet containing CHMP2AΔC-CHMP3 tubes was resuspended in buffer D. In order to wrap the CHMP2AΔC-CHMP3 tubes with a lipid bilayer, the following lipid film was produced containing 70% Egg phosphatidyl choline (Egg PC), 10% dioleoyl glycero phosphoserine (DOPS), 10% dioleoyl glycerol phosphoethanolamine (DOPE), 10% brain phosphatidylinositol-4,5-bisphosphate (PI(4,5)P2) and 2µL of dioleoyl-sn-glycero-3-phosphoethanolamine-N-(lissamine rhodamine B sulfonyl) (LISS-Rhodamin PE) (all Avanti Polar lipids). The lipid film was re-suspended in water at a final concentration of 5 mg/mL. The CHMP2AΔC-CHMP3 tubes (25 µL) were mixed with 25 µL of 2% CHAPS, 25 µL of lipids and 0.1 mg/mL of TEV protease (to remove the MBP from CHMP2AΔC) and incubated at room temperature for 2h. To remove free lipids/micelles and CHAPS, the tubes were dialyzed twice for 48-72h against buffer I (25mM Tris pH 7.4, 25 mM NaCl, 1 mM β-mercaptoethanol and 0.5 g of Bio-Beads (Biorad). After dialysis, CHMP2AΔC-CHMP3 tubes wrapped with bilayer were incubated with Bio-Beads overnight at 4°C and removed by centrifugation. The removal of CHAPS was monitored by UV spectroscopy. The quality of the bilayer wrapped CHMP2AΔC-CHMP3 tubes was assessed by negative staining EM prior to cryo-EM data collection, fluorescence microscopy imaging and HS-AFM analysis.

To test remodeling by VPS4, CHMP2A-CHMP3 tubes were incubated with 10 to 20 µM VPS4B, 5 mM $MgCl_2$ and 5 or 10 mM caged ATP (#A1048 Invitrogen) prior to membrane wrapping, following the protocol described above. Because deposition of the membrane onto the CHMP2A-CHMP3 protein coat requires extensive dialysis, the final VPS4 concentration present within the tubes can be only estimated from SDS-PAGE; however, the final concentration of caged ATP inserted into the tubes cannot be determined.

CHMP2A-CHMP3-VPS4 membrane tube imaging

Epifluorescence video microscopy of CHMP2A-CHMP3 membrane tubes containing VPS4B and caged ATP was performed using an Olympus IX83 optical microscope equipped with a UPFLN 100X O-2PH/1.3 objective and an ORCA-Flash4.0 Digital sCMOS camera (Hamamatsu). A 5 µL aliquot of ESCRT-III tube suspension was spread on a slide, covered with a glass coverslip (#1) and sealed with twinsil speed 22 (Picodent, ref 13001002) for imaging. Caged-ATP was uncaged using a 10s 10% 365-nm LED illumination (**Fig. 5a-f; movies 1-4**) or using at each time point a 100ms 30% 365-nm LED illumination (**Extended Data Fig. 9; movies 5 and 6**). ESCRT tubes were fluorescently imaged using a 550 nm LED (10% with an exposure time of 100 ms) at 1 frame/s. Images were acquired using the Volocity software package. Images were analyzed, adjusted, and cropped using ImageJ software.

HS-AFM analysis

The AFM images were acquired in amplitude modulation tapping mode in liquid, using high-speed atomic force microscopes (RIBM, Japan) [56,76]. The HS-AFM imaging was performed using USC-F1.2-k0.15 cantilevers (NanoWorld, Switzerland), an ultrashort cantilever with a nominal spring constant of 0.15 N/m and a resonance frequency ≈ 0.5 MHz. All HS-AFM recordings were done at room temperature and in buffer D. Uncaging of the caged ATP was performed by directly irradiating 365 nm UV light at the AFM sample stage using an optical fiber. The membrane coated tubes were immobilized at the surface using streptavidin on top of a lipid bilayer (DOPC) on mica containing 0.01% biotinylated lipid [77]. HS-AFM images were analyzed using Igor Pro, and ImageJ with additional home written plugins [78]. Height measurements were performed on raw images after tilt correction.

Dominant negative effect of CHMP3(1-150) wild type and mutants

CHMP3 residues 1-150 wt or mutants were synthesized (ThermoFisher) and cloned into the pEGFP-N1 vector using restriction sites *Xho*1- *Hind*III. To determine the effect of CHMP3(1-150)-

GFP on virus like particle (VLP) production upon HIV-1 Gag expression, 293T cells were seeded into 10mm dishes and transfected 24 hr later using a Jetprime (Polyplus) technique. The cultures were co-transfected with 0.5 µg of Rev-independent HIV-1 Gag construct and with 2 µg of either pcDNA or wild type and mutant versions of CHMP3(1-150)-GFP. Twenty-four hours post transfection, VLPs released into the culture medium were pelleted through sucrose. HIV-1 Gag proteins in VLPs and cell lysates were detected by Western blotting with a mouse anti-p24 antibody (183-H12-5C). For life cell imaging cells were seeded in glass bottomed µ-dishes and co-transfected with 0.8 µg of Rev-independent HIV-1 Gag construct, 0.2 µg of Gag-mCherry [79] and with 1 µg of either wild type or mutant CHMP3(1-150)-GFP. ESCRT-III and Gag protein localization was analyzed by spinning disc confocal microscopy 24 hr post transfection in HeLA cells.

Cryo-EM sample preparation and data collection

Cryo-electron microscopy. 3.5 µL of sample were applied to glow discharged (45s 30 mA) 1.2/1.3 Ultrafoil holey grids (Quantifoil Micro Tools GmbH, Germany) and they were plunged frozen in liquid ethane with a Vitrobot Mark IV (Thermo Fisher Scientific) (100% humidity, temperature 20°C, 6 s blot time, blot force 0). The grids were pre-screened on the 200kV Glacios electron microscope (Thermo Fischer Scientific) at the IBS (Grenoble) and data were collected at the beamline CM01 of the ESRF (Grenoble, France) [80] on a Titan Krios G3 (Thermo Fischer Scientific) at 300 kV equipped with an energy filter (Bioquantum LS/967, Gatan Inc, USA) (slit width of 20 eV). 5028 movies were recorded automatically on a K2 summit direct detector (Gatan Inc., USA) with EPU (Thermo Fisher Scientific) for a total exposure time of 5 s and 200 ms per frame resulting in 25 frame movies with a total dose of ~24 $e^-/Å^2$. The magnification was 130,000x (1.052 Å/pixel at the camera level). The defocus of the images was adjusted between −0.5 and −1.5 µm in 0.2 µm steps. For the high ionic strength unwinding of the CHMP2A-CHMPA filament the same grid and freezing conditions have been used as described above and images have been recorded on the Glacios electron microscope using a K2 direct electron detector.

EM image analysis and 3D reconstructions

The workflow of the image analysis is shown in **Extended Data Fig.2**. Electron beam-induced sample motion on the recorded movie frames was corrected using MotionCor2 [81] and the contrast transfer function (CTF) was estimated with CTFFIND4 [82]. 9,207 filaments were manually picked from 5,027 micrographs using the EMAN2 program e2helixboxer.py [83]. All subsequent data processing steps were carried out in RELION3 [84,85] unless mentioned otherwise. Initially, 89,122

overlapping segments were extracted with ~90% overlap between boxes of 768 x 768 pixels and down sampled to a pixel size of 2.104 for initial classification steps. Several rounds of 2D classification resulted in class averages that could be classified into 5 main different groups based on the filament diameter, without membrane (380 Å diameter (7.4%), 410 Å diameter (51.4%), 430 Å diameter (31.2%), 470 Å diameter (1.9%) and 490 Å diameter (0.3%)). In order to compensate for potential mis-assignment of diameters to the segments due to inaccuracies in 2D classification, we assigned to each entire tube a diameter based on the class assignment of the corresponding segments. If more than 80% of segments of a particular tube were belonging to classes assigned to a particular diameter, this entire tube would be assigned this diameter for the subsequent steps. After re-extraction of segments with ~95% overlap, another round of 2D classification was performed for each diameter group. Most populated 2D classes with filament diameter of 430 Å and 410 Å were chosen for further processing and analysis. For determination of helical symmetry, the sum of power spectra from a smaller subset (1,904 and 3,993 segments from one 2D class each for 430 Å and 410 Å respectively) was calculated for both filament groups. The resulting average power spectrum (**Extended Data Fig.1c and d**) was analyzed for estimation of helical symmetry parameters using the web tool helixplorer (http://rico.ibs.fr/helixplorer/). Based on a prior visual inspection of the Power Spectrum, we made following hypotheses: the layer line with a maximum seemingly on the meridian could be the helical rise or the pitch (given the large diameter of the tube and possibilities that selected 2D class averages contained a number of slightly out-of-plane tilted segments). Given those two hypotheses, and allowing any cyclic symmetries, we explored possible helical symmetries matching the experimental PS, giving a list of 20 and 15 symmetries to test for the 430 Å and 410 Å diameter classes, respectively. Those symmetries were applied on the real-space 2D class-averages using SPRING program segclassreconstruct.py [86] in order to generate initial models and narrowing down possible symmetry solutions to 14 and 10, by discarding those giving aberrant density distribution. Using those initial models, each of the remaining symmetry solutions was tested for 3D refinement in RELION3, and the resulting maps inspected for high-resolution features such as clear secondary structures, allowing to determine the helical parameters to be 18 Å pitch, 2.72 Å rise, 54.39° twist, 6.6 units/turn and C2 point symmetry for 430 Å, and 9 Å pitch, 1.43 Å rise, 57° twist, 6.3 units/turn and C1 point symmetry for 410 Å diameter filaments.

In order to select a more homogeneous subset of segments, we applied 3D classification and the classes (containing 25,353 and 11,396 segments for diameters 430 and 410 Å) were chosen for a final round of 3D auto-refine reconstruction that converged to a 2.74 Å rise and 54.37° twist for 430 Å, and 1.44 Å rise and 57.04° twist for 410 Å diameter filaments. Using soft protein-only

masks, the final resolutions were estimated at 3.3 Å and 3.6 Å for the 430 Å and 410 Å diameter filaments, at the FSC (Fourier shell correlation) 0.143 cutoff criterion [87]. The maps were sharpened with B factors of -96.57 Å^2 (430 Å) and -101.52 Å^2 (410 Å). Local resolution was estimated in RELION 3 [84] and the density maps were rendered in UCSF Chimera [88]. The statistics of the EM map are summarized in **Table 1**.

Membrane thickness was measured from the 2D class averages of membrane-bound CHMP2A-CHMP3 tubes as well as protein-free membrane vesicles generated during the membrane-coating process and plotted using the GraphPad Prism 5 software package. The statistical significance was determined using the t-test. For membrane-bound CHMP2A-CHMP3 tubes, measurements were made using several 2D classes of both 430 Å and 410 Å diameter tubes. For protein-free membrane, 257 particles were manually picked from the same set of cryo-EM micrographs that were used for CHMP2A-CHMP3 membrane tube reconstruction. 2D classification was performed using RELION 3 [84] and membrane thickness was measured from 2D class averages. 30 measurements were made for each set. A mean thickness of 59.2 Å was observed for the protein-free membrane as compared to 49.8 Å for CHMP2A-CHMP3 bound membrane. Thus, a shrinkage of ~9 Å was observed in the membrane thickness upon CHMP2A-CHMP3 binding.

Atomic modelling and validation

The SWISS-MODEL [89] server was used to create homology models of human CHMP3 and CHMP2A, using the open conformation of CHMP1B (PDB ID 6TZ4) as a reference model. Helices with residues 15-52, 57-117 and 120-151 for CHMP3 and 14-51, 56-116 and 119-150 for CHMP2A were initially fit into the EM density as separate rigid bodies using Chimera and then adjusted in Coot [90]. Further, the rest of the N-terminal and C-terminal residues, as well as the connecting loops were manually built and adjusted in Coot. The CHMP2A-CHMP3 heterodimer model was then expanded by helical symmetry in each direction in order to get 10 such dimers surrounding the central dimer. Thus, a total of 11 helical symmetry-related dimers were again checked in Coot, before applying the first round of real-space refinement in PHENIX [91] with non-crystallographic symmetry (NCS) restraints. NCS, along with SS (secondary structure) restraints were then used for a second round of real-space refinement. At last, the symmetry-related dimers were removed and the central CHMP2A-CHMP3 dimer was saved as the final model. The statistics of the final models were tabulated using MolProbity [92] and are summarized in **Table 1** and map versus atomic model FSC plots were computed in PHENIX [93]. All structure figures were generated with UCSF Chimera, ChimeraX [94] and PyMOL (W. Delano; The PyMOL Molecular Graphics System, Version

1.8 Schrödinger, LLC, http://www.pymol.org). Sequence alignments were performed with Clustal Omega [95] and ESPript [96].

Data Availability

Cryo-EM maps and models were deposited to the PDB and EMDB with the following codes: membrane-bound CHMP2A-CHMP3, 430 Å diameter (PDB ID 7ZCG, EMD-14630) and membrane-bound CHMP2A-CHMP3, 410 Å diameter (PDB ID 7ZCH, EMD-14631).

Acknowledgement

This research was funded by the ANR (ANR-14-CE09-0003-01; ANR-19-CE11-0002-02; WW). WW acknowledges support from the Institut Universitaire de France (IUF) and access to the platforms of the Grenoble Instruct-ERIC center (IBS and ISBG; UAR 3518 CNRS-CEA-UGA-EMBL) within the Grenoble Partnership for Structural Biology (PSB), with support from FRISBI (ANR-10-INBS-05-02) and GRAL, a project of the University Grenoble Alpes graduate school (Ecoles Universitaires de Recherche) CBH-EUR-GS (ANR-17-EURE-0003). The IBS electron microscope facility is supported by the Auvergne-Rhône-Alpes Region, the Fondation pour la Recherche Medicale (FRM), the FEDER/ERDF fund (European Regional Development Fund) and the GIS-IBiSA (Infrastructures en Biologie, Sante et Agronomie). We acknowledge the provision of in-house experimental time from the CM01 facility at the ESRF and we thank Leandro Estrozi for extensive discussion and help with helical image analysis. We further thank the HIV Reagent Program, Division of AIDS, NIAID, NIH for providing the Anti-Human Immunodeficiency Virus 1 (HIV-1) p24 Monoclonal (183-H12-5C), ARP-3537, contributed by Dr. Bruce Chesebro and Kathy.

Author contributions: W.W. conceived the study, designed experiments, interpreted experiments, supervised and received funding for the study. K.A. performed all cryo-EM data analyses. N.D.F. established the membrane coating protocol. D.G. prepared wild type and mutant CHMP2A-CHMP3 polymers for all analyses. G.Su. (G. Sulbaran) performed negative staining EM analyses. C.B. and J.P.K. performed fluorescence microscopy imaging and H.W. mutant analyses. S.M. performed AFM analyses and W.H.R. supervised AFM analyses. G.E. and G.S. collected cryoEM data and A.D. supervised all aspects of cryoEM data analyses and structure solution. W.W. wrote the paper with input from all authors.

Competing interests: The authors declare no competing interests.

References

1. Henne, W.M., Stenmark, H. & Emr, S.D. Molecular mechanisms of the membrane sculpting ESCRT pathway. *Cold Spring Harb Perspect Biol* **5**, a016766 (2013).
2. Votteler, J. & Sundquist, W.I. Virus budding and the ESCRT pathway. *Cell Host Microbe* **14**, 232-41 (2013).
3. Allison, R. et al. An ESCRT-spastin interaction promotes fission of recycling tubules from the endosome. *J Cell Biol* **202**, 527-43 (2013).
4. Loncle, N., Agromayor, M., Martin-Serrano, J. & Williams, D.W. An ESCRT module is required for neuron pruning. *Sci Rep* **5**, 8461- (2015).
5. Olmos, Y. & Carlton, J.G. The ESCRT machinery: new roles at new holes. *Curr Opin Cell Biol* **38**, 1-11 (2016).
6. Scourfield, E.J. & Martin-Serrano, J. Growing functions of the ESCRT machinery in cell biology and viral replication. *Biochem Soc Trans* **45**, 613-634 (2017).
7. Sadoul, R. et al. The role of ESCRT during development and functioning of the nervous system. *Semin Cell Dev Biol* **74**, 40-49 (2018).
8. Mast, F.D. et al. ESCRT-III is required for scissioning new peroxisomes from the endoplasmic reticulum. *J Cell Biol* **217**, 2087-2102 (2018).
9. Zhen, Y., Radulovic, M., Vietri, M. & Stenmark, H. Sealing holes in cellular membranes. *EMBO J* **40**, e106922 (2021).
10. McCullough, J., Frost, A. & Sundquist, W.I. Structures, Functions, and Dynamics of ESCRT-III/Vps4 Membrane Remodeling and Fission Complexes. *Annu Rev Cell Dev Biol* **34**, 85-109 (2018).
11. Bertin, A. et al. Human ESCRT-III polymers assemble on positively curved membranes and induce helical membrane tube formation. *Nat Commun* **11**, 2663 (2020).
12. Moser von Filseck, J. et al. Anisotropic ESCRT-III architecture governs helical membrane tube formation. *Nat Commun* **11**, 1516 (2020).
13. Caillat, C., Maity, S., Miguet, N., Roos, W.H. & Weissenhorn, W. The role of VPS4 in ESCRT-III polymer remodeling. *Biochem Soc Trans* **47**, 441-448 (2019).
14. Liu, J. et al. Bacterial Vipp1 and PspA are members of the ancient ESCRT-III membrane-remodeling superfamily. *Cell* **184**, 3660-3673 (2021).
15. Junglas, B. et al. PspA adopts an ESCRT-III-like fold and remodels bacterial membranes. *Cell* **184**, 3674-3688 (2021).
16. Pfitzner, A.K., Moser von Filseck, J. & Roux, A. Principles of membrane remodeling by dynamic ESCRT-III polymers. *Trends Cell Biol* **31**, 856-868 (2021).
17. Nguyen, H.C. et al. Membrane constriction and thinning by sequential ESCRT-III polymerization. *Nat Struct Mol Biol* **27**, 392-399 (2020).
18. Remec Pavlin, M. & Hurley, J.H. The ESCRTs - converging on mechanism. *J Cell Sci* **133**, jcs240333 (2020).
19. Harker-Kirschneck, L. et al. Physical mechanisms of ESCRT-III-driven cell division. *Proc Natl Acad Sci U S A* **119**, e2107763119 (2022).
20. Babst, M., Katzmann, D.J., Estepa-Sabal, E.J., Meerloo, T. & Emr, S.D. ESCRT-III: An endosome-associated heterooligomeric protein complex required for MVB sorting. *Dev Cell* **3**, 271-282 (2002).
21. Morita, E. et al. ESCRT-III Protein Requirements for HIV-1 Budding. *Cell Host Microbe* **9**, 235-42 (2011).
22. Teis, D., Saksena, S. & Emr, S.D. Ordered Assembly of the ESCRT-III Complex on Endosomes Is Required to Sequester Cargo during MVB Formation. *Dev Cell* **15(4)**, 578-89. (2008).
23. Saksena, S., Wahlman, J., Teis, D., Johnson, A.E. & Emr, S.D. Functional reconstitution of ESCRT-III assembly and disassembly. *Cell* **136**, 97-109 (2009).

24. Zamborlini, A. et al. Release of autoinhibition converts ESCRT-III components into potent inhibitors of HIV-1 budding. *Proc Natl Acad Sci U S A* **103**, 19140-5 (2006).
25. Rheinemann, L. et al. RetroCHMP3 blocks budding of enveloped viruses without blocking cytokinesis. *Cell* **184**, 5419-5431 (2021).
26. Effantin, G. et al. ESCRT-III CHMP2A and CHMP3 form variable helical polymers in vitro and act synergistically during HIV-1 budding. *Cell Microbiol* **15**, 213-26 (2013).
27. Schoneberg, J. et al. ATP-dependent force generation and membrane scission by ESCRT-III and Vps4. *Science* **362**, 1423-1428 (2018).
28. Muziol, T. et al. Structural basis for budding by the ESCRT-III factor CHMP3. *Dev Cell* **10**, 821-30 (2006).
29. Bajorek, M. et al. Structural basis for ESCRT-III protein autoinhibition. *Nat Struct Mol Biol* **16**, 754-62 (2009).
30. Xiao, J. et al. Structural basis of Ist1 function and Ist1-Did2 interaction in the multivesicular body pathway and cytokinesis. *Mol Biol Cell* **20**, 3514-24 (2009).
31. Im, Y.J., Wollert, T., Boura, E. & Hurley, J.H. Structure and function of the ESCRT-II-III interface in multivesicular body biogenesis. *Dev Cell* **17**, 234-43 (2009).
32. Pineda-Molina, E. et al. The crystal structure of the C-terminal domain of Vps28 reveals a conserved surface required for Vps20 recruitment. *Traffic* **7**, 1007-16 (2006).
33. McCullough, J., Fisher, R.D., Whitby, F.G., Sundquist, W.I. & Hill, C.P. ALIX-CHMP4 interactions in the human ESCRT pathway. *Proc Nat Acad Sci USA* **105**, 7687-7691 (2008).
34. Tang, S. et al. ESCRT-III activation by parallel action of ESCRT-I/II and ESCRT-0/Bro1 during MVB biogenesis. *Elife* **5**, e15507 (2016).
35. Shim, S., Kimpler, L.A. & Hanson, P.I. Structure/Function Analysis of Four Core ESCRT-III Proteins Reveals Common Regulatory Role for Extreme C-Terminal Domain. *Traffic* **8**, 1068-1079 (2007).
36. Lata, S. et al. Structural basis for autoinhibition of ESCRT-III CHMP3. *J Mol Biol* **378**, 818-27 (2008).
37. McCullough, J. et al. Structure and membrane remodeling activity of ESCRT-III helical polymers. *Science* **350**, 1548-51 (2015).
38. Cada, A.K. et al. Reconstitution reveals friction-driven membrane scission by the human ESCRT-III proteins CHMP1B and IST1. *bioRxiv* **2022.02.03.479062**(2022).
39. Tang, S. et al. Structural basis for activation, assembly and membrane binding of ESCRT-III Snf7 filaments. *Elife* **4**, e12548 (2015).
40. McMillan, B.J. et al. Electrostatic Interactions between Elongated Monomers Drive Filamentation of Drosophila Shrub, a Metazoan ESCRT-III Protein. *Cell Rep* **16**, 1211-1217 (2016).
41. Pires, R. et al. A crescent-shaped ALIX dimer targets ESCRT-III CHMP4 filaments. *Structure* **17**, 843-56 (2009).
42. Chiaruttini, N. et al. Relaxation of Loaded ESCRT-III Spiral Springs Drives Membrane Deformation. *Cell* **163**, 866-79 (2015).
43. Mierzwa, B.E. et al. Dynamic subunit turnover in ESCRT-III assemblies is regulated by Vps4 to mediate membrane remodelling during cytokinesis. *Nat Cell Biol* **19**, 787-798 (2017).
44. Lee, I.H., Kai, H., Carlson, L.A., Groves, J.T. & Hurley, J.H. Negative membrane curvature catalyzes nucleation of endosomal sorting complex required for transport (ESCRT)-III assembly. *Proc Natl Acad Sci U S A* **112**, 15892-7 (2015).
45. Hanson, P.I., Roth, R., Lin, Y. & Heuser, J.E. Plasma membrane deformation by circular arrays of ESCRT-III protein filaments. *J Cell Biol.* **180(2)**, 389-402 (2008).
46. Cashikar, A.G. et al. Structure of cellular ESCRT-III spirals and their relationship to HIV budding. *Elife*, e02184 (2014).

47. Gupta, T.K. et al. Structural basis for VIPP1 oligomerization and maintenance of thylakoid membrane integrity. *Cell* **184**, 3643-3659 (2021).
48. Lata, S. et al. Helical structures of ESCRT-III are disassembled by VPS4. *Science* **321**, 1354-7 (2008).
49. Moriscot, C. et al. Crenarchaeal CdvA forms double-helical filaments containing DNA and interacts with ESCRT-III-like CdvB. *PLoS ONE* **6**, e21921 (2011).
50. Dobro, M.J. et al. Electron cryotomography of ESCRT assemblies and dividing Sulfolobus cells suggests that spiraling filaments are involved in membrane scission. *Mol Biol Cell* **24**, 2319-27 (2013).
51. Henne, W.M., Buchkovich, N.J., Zhao, Y. & Emr, S.D. The Endosomal Sorting Complex ESCRT-II Mediates the Assembly and Architecture of ESCRT-III Helices. *Cell* **151**, 356-371 (2012).
52. Bodon, G. et al. Charged Multivesicular Body Protein 2B (CHMP2B) of the Endosomal Sorting Complex Required for Transport-III (ESCRT-III) Polymerizes into Helical Structures Deforming the Plasma Membrane. *J Biol Chem* **286**, 40276-40286 (2011).
53. Guizetti, J. et al. Cortical Constriction During Abscission Involves Helices of ESCRT-III-Dependent Filaments. *Science* **331**, 1616-20 (2011).
54. Sherman, S. et al. Resolving new ultrastructural features of cytokinetic abscission with soft-X-ray cryo-tomography. *Sci Rep.* **6**, 27629 (2016).
55. Goliand, I. et al. Resolving ESCRT-III Spirals at the Intercellular Bridge of Dividing Cells Using 3D STORM. *Cell Rep* **24**, 1756-1764 (2018).
56. Maity, S. et al. VPS4 triggers constriction and cleavage of ESCRT-III helical filaments. *Sci Adv* **5**, eaau7198 (2019).
57. Kieffer, C. et al. Two distinct modes of ESCRT-III recognition are required for VPS4 functions in lysosomal protein targeting and HIV-1 budding. *Dev Cell* **15**, 62-73 (2008).
58. Adell, M.A. et al. Coordinated binding of Vps4 to ESCRT-III drives membrane neck constriction during MVB vesicle formation. *J Cell Biol* **205**, 33-49 (2014).
59. Adell, M.A.Y. et al. Recruitment dynamics of ESCRT-III and Vps4 to endosomes and implications for reverse membrane budding. *Elife* **6**, e31652 (2017).
60. He, S. & Scheres, S.H.W. Helical reconstruction in RELION. *J Struct Biol* **198**, 163-176 (2017).
61. Huber, S.T., Mostafavi, S., Mortensen, S.A. & Sachse, C. Structure and assembly of ESCRT-III helical Vps24 filaments. *Sci Adv* **6**, eaba4897 (2020).
62. Buchkovich, N.J., Henne, W.M., Tang, S. & Emr, S.D. Essential N-terminal insertion motif anchors the ESCRT-III filament during MVB vesicle formation. *Dev Cell* **27**, 201-214 (2013).
63. Vietri, M., Radulovic, M. & Stenmark, H. The many functions of ESCRTs. *Nat Rev Mol Cell Biol* **21**, 25-42 (2020).
64. Prescher, J. et al. Super-resolution imaging of ESCRT-proteins at HIV-1 assembly sites. *PLoS Pathog* **11**, e1004677 (2015).
65. Johnson, D.S., Bleck, M. & Simon, S.M. Timing of ESCRT-III protein recruitment and membrane scission during HIV-1 assembly. *Elife* **7**, e36221 (2018).
66. Pfitzner, A.K. et al. An ESCRT-III Polymerization Sequence Drives Membrane Deformation and Fission. *Cell* **182**, 1140-1155 (2020).
67. Banjade, S., Tang, S., Shah, Y.H. & Emr, S.D. Electrostatic lateral interactions drive ESCRT-III heteropolymer assembly. *Elife* **8**, e46207 (2019).
68. Whitley, P. et al. Identification of Mammalian Vps24p as an Effector of Phosphatidylinositol 3,5-Bisphosphate-dependent Endosome Compartmentalization. *J. Biol. Chem.* **278**, 38786-38795 (2003).
69. Lin, Y., Kimpler, L.A., Naismith, T.V., Lauer, J.M. & Hanson, P.I. Interaction of the mammalian endosomal sorting complex required for transport (ESCRT) III protein hSnf7-

1 with itself, membranes, and the AAA+ ATPase SKD1. *J. Biol. Chem.* **280**, 12799-809 (2005).
70. De Franceschi, N. et al. The ESCRT protein CHMP2B acts as a diffusion barrier on reconstituted membrane necks. *J Cell Sci* **132**, jcs217968 (2018).
71. Banjade, S., Shah, Y.H., Tang, S. & Emr, S.D. Design principles of the ESCRT-III Vps24-Vps2 module. *Elife* **10**, e67709 (2021).
72. Caillat, C. et al. Asymmetric ring structure of Vps4 required for ESCRT-III disassembly. *Nat Commun* **6**, 8781 (2015).
73. Fabrikant, G. et al. Computational model of membrane fission catalyzed by ESCRT-III. *PLoS Comput Biol* **5**, e1000575 (2009).
74. Caspi, Y. & Dekker, C. Dividing the Archaeal Way: The Ancient Cdv Cell-Division Machinery. *Front Microbiol* **9**, 174 (2018).
75. Ithurbide, S., Gribaldo, S., Albers, S.V. & Pende, N. Spotlight on FtsZ-based cell division in Archaea. *Trends Microbiol* **30**, 665-678 (2022).
76. Maity, S. et al. Caught in the Act: Mechanistic Insight into Supramolecular Polymerization-Driven Self-Replication from Real-Time Visualization. *J Am Chem Soc* **142**, 13709-13717 (2020).
77. Keya, J.J. et al. High-Resolution Imaging of a Single Gliding Protofilament of Tubulins by HS-AFM. *Sci Rep* **7**, 6166 (2017).
78. Maity, S. et al. High-speed atomic force microscopy reveals a three-state elevator mechanism in the citrate transporter CitS. *Proc Natl Acad Sci U S A* **119**, e2113927119 (2022).
79. Jouvenet, N., Bieniasz, P.D. & Simon, S.M. Imaging the biogenesis of individual HIV-1 virions in live cells. *Nature* **454**, 236-40 (2008).
80. Kandiah, E. et al. CM01: a facility for cryo-electron microscopy at the European Synchrotron. *Acta Crystallogr D Struct Biol* **75**, 528-535 (2019).
81. Zheng, S.Q. et al. MotionCor2: anisotropic correction of beam-induced motion for improved cryo-electron microscopy. *Nat Methods* **14**, 331-332 (2017).
82. Rohou, A. & Grigorieff, N. CTFFIND4: Fast and accurate defocus estimation from electron micrographs. *J Struct Biol* **192**, 216-21 (2015).
83. Tang, G. et al. EMAN2: an extensible image processing suite for electron microscopy. *J Struct Biol* **157**, 38-46 (2007).
84. Scheres, S.H. RELION: implementation of a Bayesian approach to cryo-EM structure determination. *J Struct Biol* **180**, 519-30 (2012).
85. Zivanov, J. et al. New tools for automated high-resolution cryo-EM structure determination in RELION-3. *Elife* **7**, e42166 (2018).
86. Desfosses, A., Ciuffa, R., Gutsche, I. & Sachse, C. SPRING - an image processing package for single-particle based helical reconstruction from electron cryomicrographs. *J Struct Biol* **185**, 15-26 (2014).
87. Rosenthal, P.B. & Henderson, R. Optimal determination of particle orientation, absolute hand, and contrast loss in single-particle electron cryomicroscopy. *J Mol Biol* **333**, 721-45 (2003).
88. Pettersen, E.F. et al. UCSF Chimera--a visualization system for exploratory research and analysis. *J Comput Chem* **25**, 1605-12 (2004).
89. Waterhouse, A. et al. SWISS-MODEL: homology modelling of protein structures and complexes. *Nucleic Acids Res* **46**, W296-W303 (2018).
90. Emsley, P., Lohkamp, B., Scott, W.G. & Cowtan, K. Features and development of Coot. *Acta Crystallogr D Biol Crystallogr* **66**, 486-501 (2010).
91. Adams, P.D. et al. PHENIX: a comprehensive Python-based system for macromolecular structure solution. *Acta Crystallogr D Biol Crystallogr* **66**, 213-21 (2010).

92. Williams, C.J. et al. MolProbity: More and better reference data for improved all-atom structure validation. *Protein Sci* **27**, 293-315 (2018).
93. Afonine, P.V. et al. Real-space refinement in PHENIX for cryo-EM and crystallography. *Acta Crystallogr D Struct Biol* **74**, 531-544 (2018).
94. Goddard, T.D. et al. UCSF ChimeraX: Meeting modern challenges in visualization and analysis. *Protein Sci* **27**, 14-25 (2018).
95. Goujon, M. et al. A new bioinformatics analysis tools framework at EMBL-EBI. *Nucleic Acids Res* **38**, W695-9 (2010).
96. Robert, X. & Gouet, P. Deciphering key features in protein structures with the new ENDscript server. *Nucleic Acids Res* **42**, W320-4 (2014).

Figure legends

Fig. 1: Cryo-EM structure of CHMP2A-CHMP3 membrane-coated helical polymers

(a) Density map of the reconstructed 430 Å diameter CHMP2A-CHMP3 membrane tube with the top view looking down the helical axis. The helical arrangement of CHMP2A (light blue) and CHMP3 (pink) inside the bilayer membrane (dark grey) is shown. The thickness, and the inner and outer diameter of the helical protein tube are also marked in Å.

(b) Side view of the helical polymer without the lipid membrane. One left-handed filament is indicated in orange, and the thickness of one filament and the pitch of the helical assembly are also marked.

(c) Density map of the reconstructed 410 Å diameter CHMP2A-CHMP3 membrane tube with the top view looking down the helical axis. The helical arrangement of CHMP2A (green) and CHMP3 (pink) inside the bilayer membrane (dark grey) is shown. The thickness, and the inner and outer diameter of the helical protein tube are indicated in Å.

(d) Side view of the helical polymer without the lipid membrane. One left-handed filament is indicated in orange, and the thickness of one filament and the pitch of the helical assembly are indicated.

(e) Cryo-EM density of the single repeating unit of the 430 Å diameter polymer formed by the heterodimer of CHMP2A (light blue) and CHMP3 (pink) is indicated.

(f) Ribbon representation of the atomic model of CHMP2A (light blue) - CHMP3 (pink) heterodimer.

Fig. 2: Atomic model and architecture of the CHMP2A-CHMP3 helical polymer.

(a) Ribbon diagram of Cα superposition of the closed and open CHMP3 conformations (Helix 1: pink, Helix 2: purple, Helix 3: light green, Helix 4: brown, Helix 5: red). The closed conformation model contains residues 12 to 172 and the open conformation residues 11 to 169.

(b) Three interlocked copies of CHMP2A-CHMP3 heterodimer are shown as ribbons. Helix 4 and 5 of CHMP3 (pink) interact with four subsequent protomers. Helix 4 of CHMP2A (light blue) also makes similar interactions.

Fig.3: Comparison of ESCRT-III open conformations highlights their versatile polymerization modes.

(a) Ribbon diagram of Cα superposition of CHMP2A and CHMP3 reveals an RMSD of 0.934 Å.

(b) Ribbon diagram of Cα superposition of CHMP3 with the Snf7 monomer (left panel) and with the homodimer (crystallographic dimer) (right panel), which indicates a different hairpin interaction (arrow) for the second protomer and different orientations of Snf7 helix 4.

(c) Ribbon diagram of Cα superposition of CHMP3 and CHMP1B (left panel) and the superposition of the CHMP2A-CHMP3 heterodimer onto the CHMP1B homodimer (right panel) indicate the differences in helical hairpin stacking (zoom, right panel) and orientations of the C-terminal helical arms (helices 3 to 5).

(d) Ribbon diagram of Cα superposition of CHMP3 (pink) with PspA and **(e)** with Vipp1.

(f) Ribbon diagram of Cα superposition of CHMP3 with an intermediate Vps24 conformation that forms filaments on its own.

Fig. 4: Membrane interaction of the CHMP2A-CHMP3 filament.

(a) Left panel, zoomed-in view of the membrane-bound CHMP2A-CHMP3 filament, highlighting the interface between lipid membrane (dark grey) and CHMP2A (light blue) and CHMP3 (pink). Red arrows are pointing to the N-termini of both CHMP2A and CHMP3 that are oriented towards the lipid bilayer. Right panel, the orientation of the N-termini is determined by Pro11 of CHMP2A (light blue) and CHMP3 (pink) shown with the density map.

(b) Ribbon diagram of the CHMP2A-CHMP3 heterodimer indicating the basic residues (sticks) oriented towards the membrane. Basic residues conserved in yeast Vps2 and Vps24 are marked by asterisks.

(c) Electrostatic potential map of the CHMP2A-CHMP3 filament (left panel, tilted, side view), revealing the exposure of the cluster of basic charges, a small negatively charged surface and a neutral surface to the membrane. Right panel, zoomed-in view of the electrostatic surface of the inside of the polymer showing clusters of negative charges in one filament juxtaposed to positive charges of the neighboring filament.

(d) Close-up of the inter-filament interactions. Ribbon diagram of two neighboring filaments showing the basic and acidic residues of CHMP2A (left panel) and CHMP3 (right panel) implicated in electrostatic inter-filament interactions.

Fig. 5: Fluorescence microscopy imaging of CHMP2A-CHMP3 membrane tube cleavage by VPS4/ATP.

(a) A CHMP2A-CHMP3-caged ATP containing membrane coated tube was activated at 365 nm (10%, 10s) to uncage ATP and imaged over 300s (snapshots from **movie 1**). Scale bar, 1μm.

(b) The kymograph of the tube shows that the tube stays intact over the imaging time.

(c) A CHMP2A-CHMP3-VPS4B containing membrane coated tube was activated at 365 nm (10%, 10s) to uncage ATP and imaged over 300s (snapshots from **movie 3**) Scale bar, 1μm.

(d) The kymograph of the tube shows that the tube stays intact over the imaging time. **(a)** to **(d)** demonstrate that imaging at 550 nm to visualize the membrane tube and ATP uncaging at 365 nm did not change the tube structures.

(e) Imaging of a CHMP2A-CHMP3-VPS4B-caged ATP containing membrane-coated tubes following ATP uncaging (365 mm, 10%, 10s) reveals constriction and cleavage of the tube at 30 s followed by a shrinking event from both sides. Another shrinking event is observed at 40s. Eventually all tubes were disassembled at 271 s (snapshots from **movie 4**). Scale bar, 1μm.

(f) The kymograph of the tube indicates the kinetics of cleavage and shrinking.

Fig. 6. HS-AFM imaging of CHMP2A-CHMP3 membrane tube cleavage by VPS4/ATP.

(a) Snapshots of HS-AFM images (from **movie 8**) of CHMP2A-CHMP3 tubes coated with membrane and loaded with 5 μM VPS4B, 10 mM caged ATP, in absence of UV irradiation. Scale bar, 200 nm.

(b) Snapshots of HS-AFM images (from **movie 9**) of CHMP2A-CHMP3 tubes coated with membrane and loaded with 5 μM VPS4B, 10 mM caged ATP taken upon UV irradiation. Scale bar, 200 nm.

(c) Kymograph representation of the height vs time along the two lines (blue and red) in panel **b** (leftmost image) throughout movie 9.

(d) Example of height vs time profile of the membrane coated tube in absence of UV irradiation (in black, measurements are from the tube shown in **a**), and in presence of UV irradiation (in blue and red, tubes and kymographs shown in **b** and **c**).

Cryo-EM data collection, refinement and validation statistics

	Membrane-bound CHMP2A-CHMP3 (Tube Diameter 430 Å) (EMDB-14630) (PDB 7ZCG)	Membrane-bound CHMP2A-CHMP3 (Tube Diameter 410 Å) (EMDB-14631) (PDB 7ZCH)
Data collection and processing		
Magnification	130,000x	130,000x
Voltage (kV)	300	300
Electron exposure (e–/Å^2)	24	24
Defocus range (μm)	0.5-1.5	0.5-1.5
Pixel size (Å)	1.052	1.052
Symmetry imposed	C2	C1
Initial particle images (no.)	45,847	80,524
Final particle images (no.)	25,353	11,396
Map resolution (Å)	3.3	3.6
FSC threshold	0.143	0.143
Map resolution range (Å)	3.28-4.58	3.64-5.21
Refinement		
Initial model used (PDB code)	*de novo*	*de novo*
Model resolution (Å)	3.6	4.0
FSC threshold	0.5	0.5
Model resolution range (Å)	2.8-3.6	2.9-4.0
Map sharpening *B* factor (Å^2)	-96.57	-101.52
Model composition		
Non-hydrogen atoms	27,148	27,148
Protein residues	3,366	3,366
Ligands	0	0
B factors (Å^2)		
Protein	74.18	90.17
Ligand	-	-
R.m.s. deviations		
Bond lengths (Å)	0.004	0.004
Bond angles (°)	0.758	0.762
Validation		
MolProbity score	1.86	1.89
Clashscore	15.23	21.23
Poor rotamers (%)	0	0
Ramachandran plot		
Favored (%)	97.02	97.68
Allowed (%)	2.98	2.32
Disallowed (%)	0	0

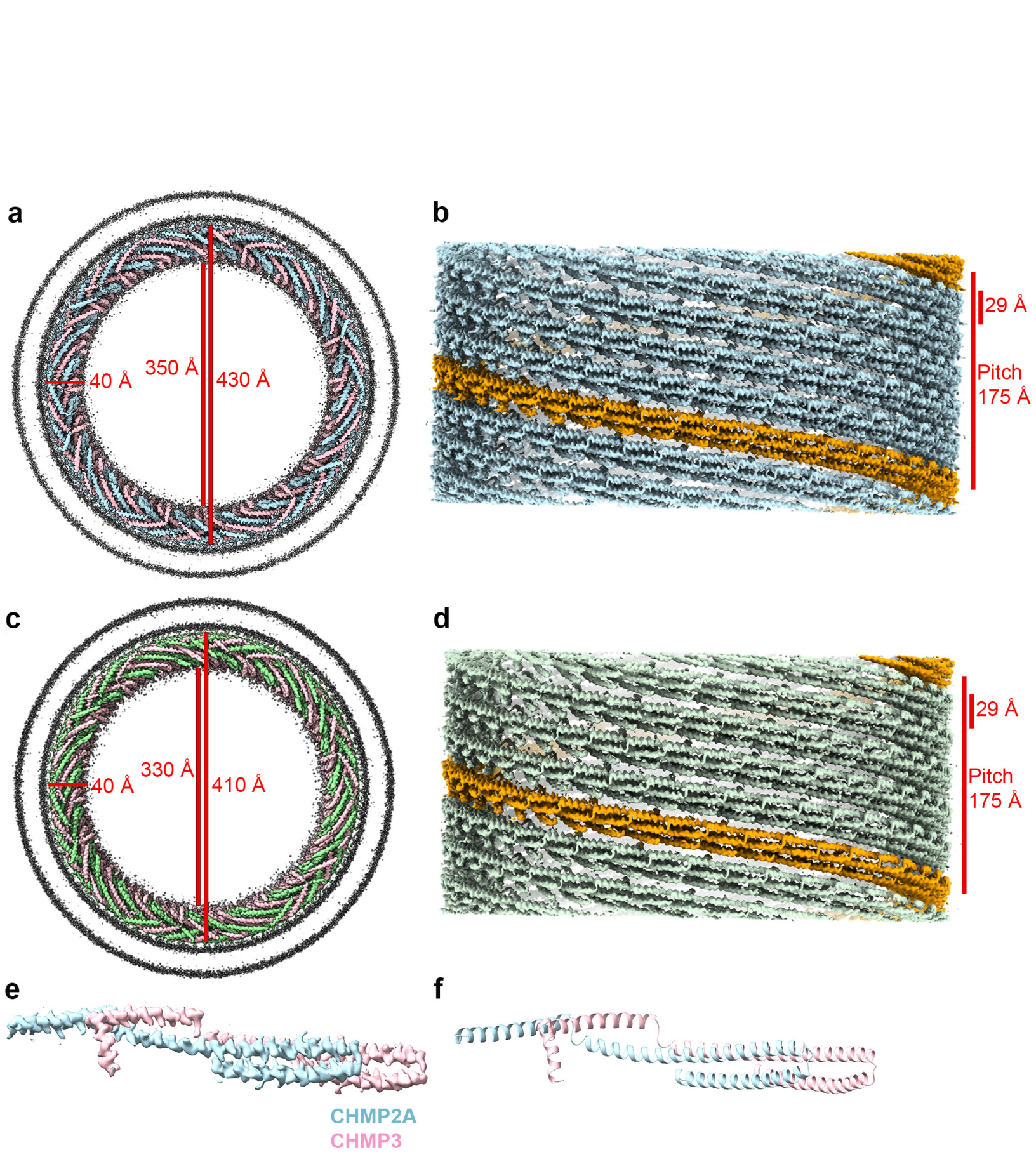
a
40 Å
350 Å
430 Å
b
29 Å
Pitch
175 Å
c
40 Å
330 Å
410 Å
d
29 Å
Pitch
175 Å
e
CHMP2A
CHMP3
f

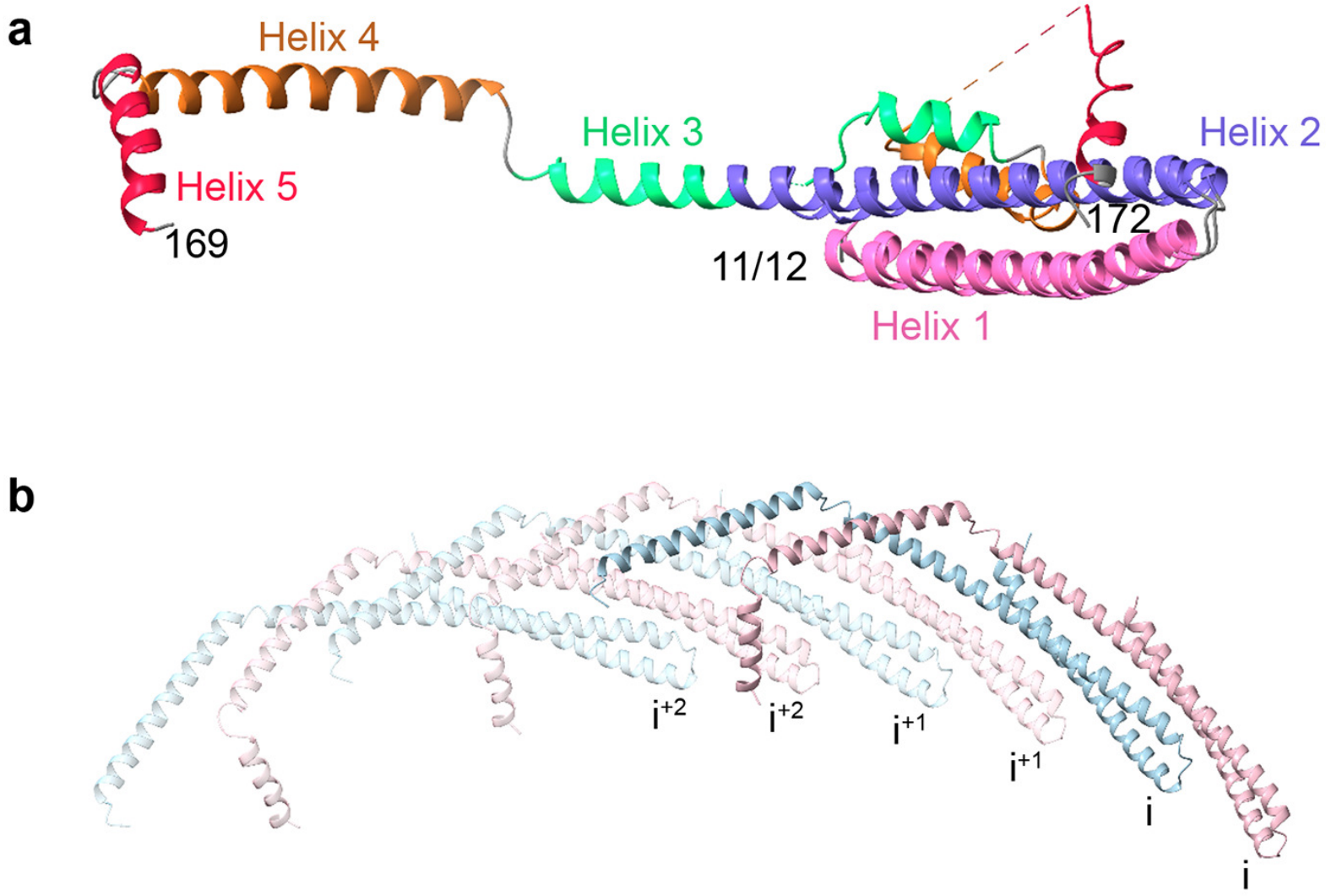
a
Helix 4
Helix 5
169
Helix 3
Helix 2
172
11/12
Helix 1
b
i+2
i+2
i+1
i+1
i
i

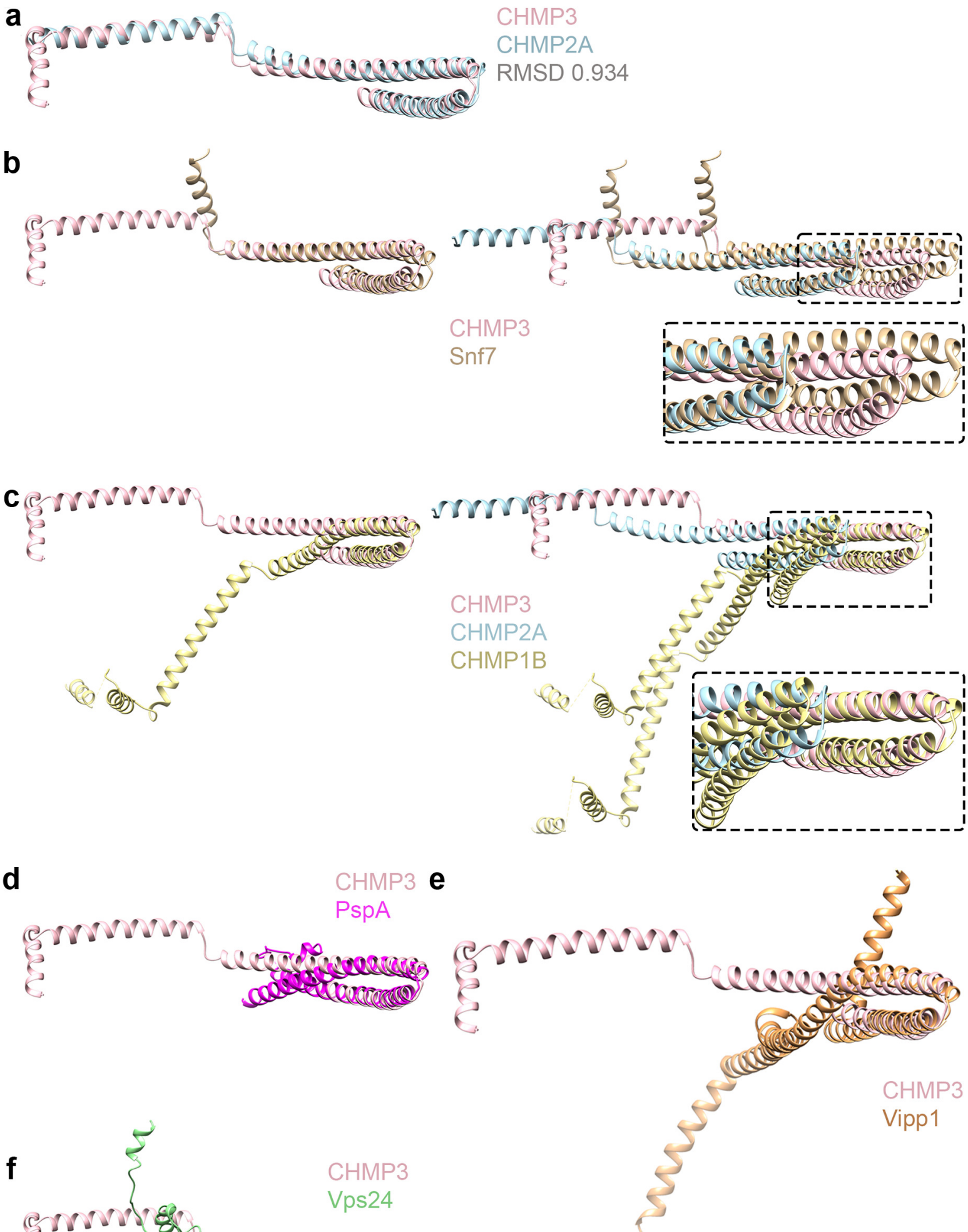
a
CHMP3
CHMP2A
RMSD 0.934
b
CHMP3
Snf7
c
CHMP3
CHMP2A
CHMP1B
d
CHMP3
PspA
e
CHMP3
Vipp1
f
CHMP3
Vps24

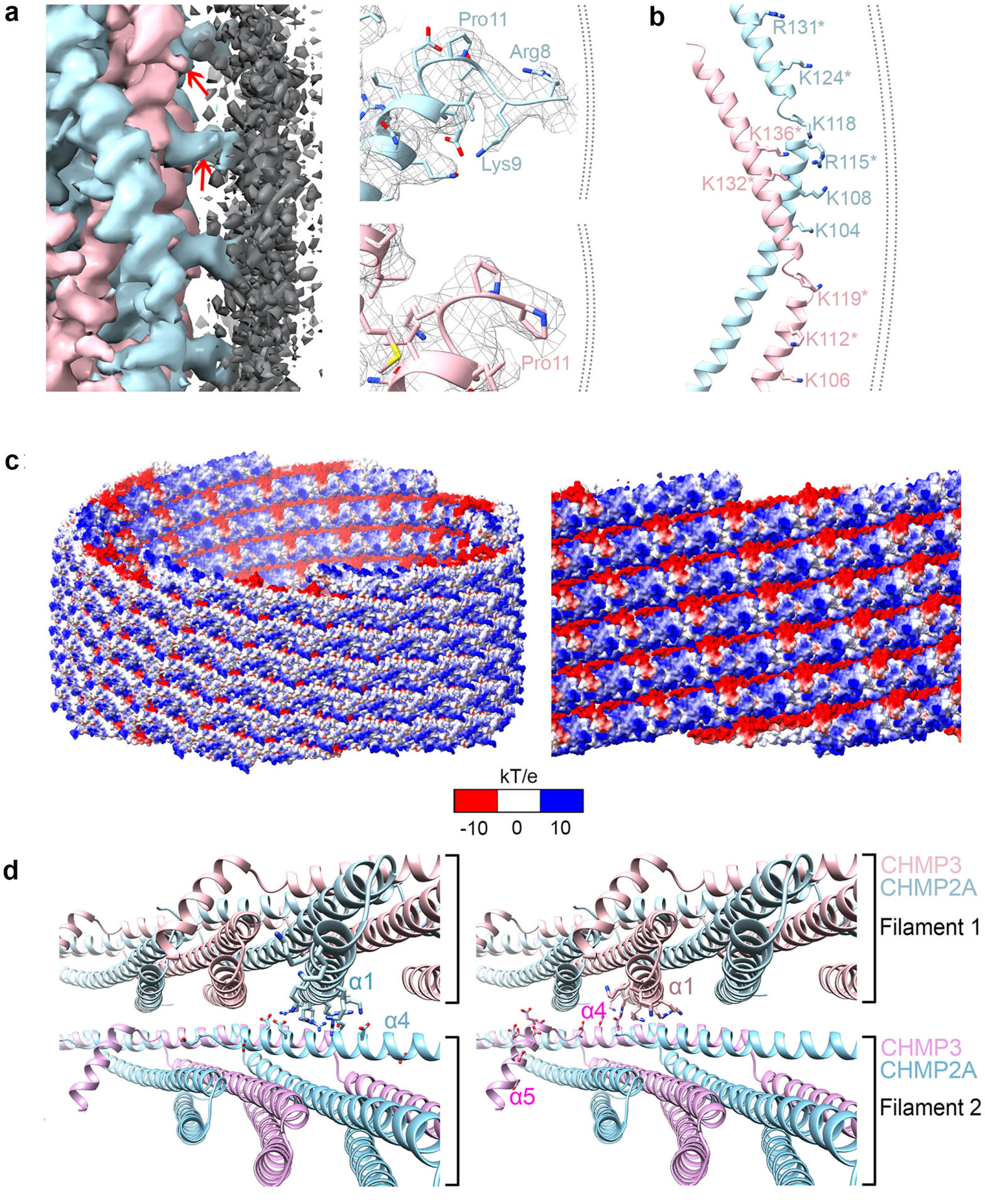
a
Pro11
Arg8
Lys9
Pro11
b
R131*
K124*
K118
K136*
R115*
K132*
K108
K104
K119*
K112*
K106
c
kT/e
-10
0
10
d
α1
α4
α1
α4
α5
CHMP3
CHMP2A
Filament 1
CHMP3
CHMP2A
Filament 2

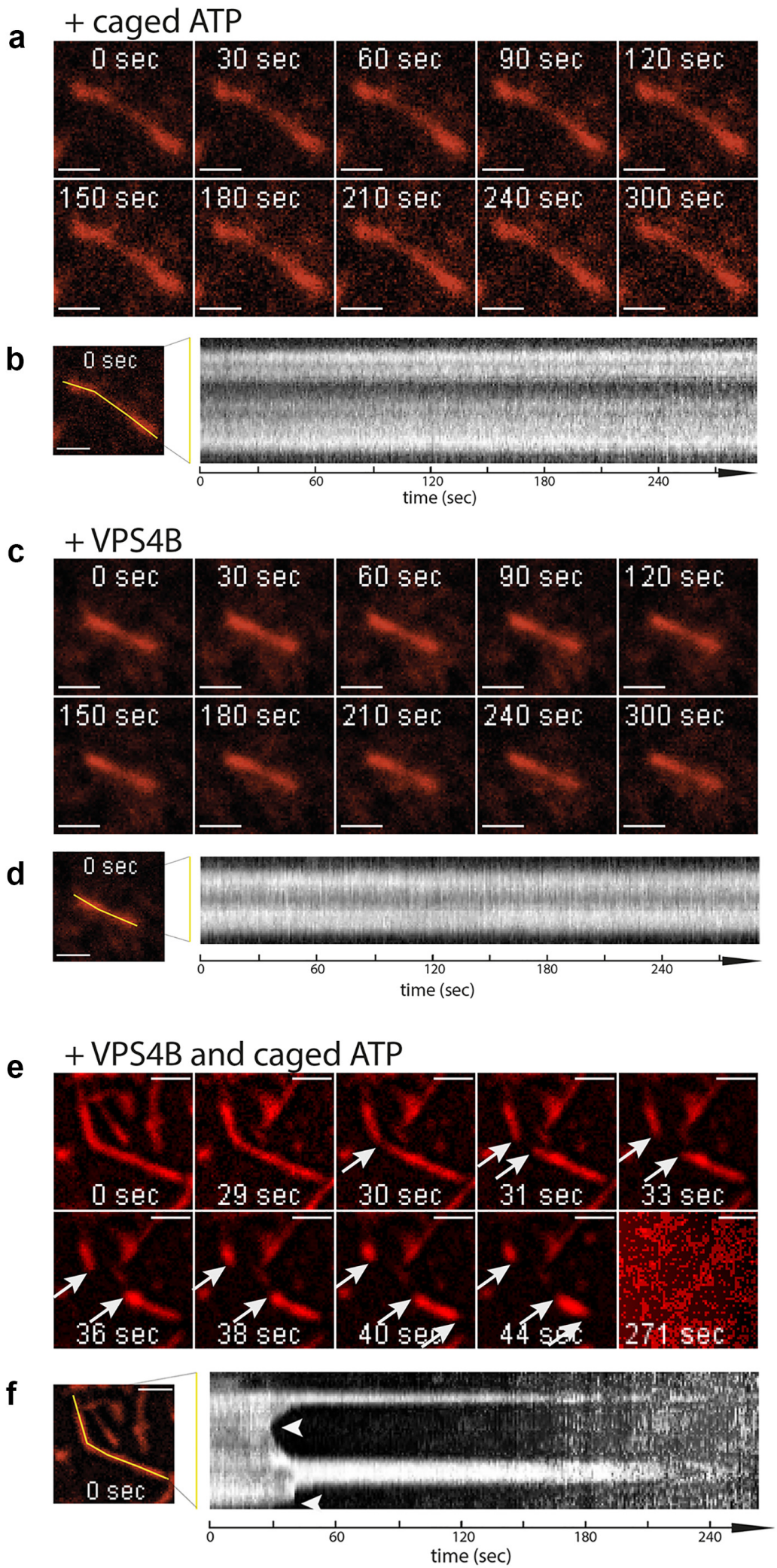
a
+ caged ATP
0 sec
30 sec
60 sec
90 sec
120 sec
150 sec
180 sec
210 sec
240 sec
300 sec
b
0 sec
0
60
120
180
240
time (sec)
c
+ VPS4B
0 sec
30 sec
60 sec
90 sec
120 sec
150 sec
180 sec
210 sec
240 sec
300 sec
d
0 sec
0
60
120
180
240
time (sec)
e
+ VPS4B and caged ATP
0 sec
29 sec
30 sec
31 sec
33 sec
36 sec
38 sec
40 sec
44 sec
271 sec
f
0 sec
0
60
120
180
240
time (sec)

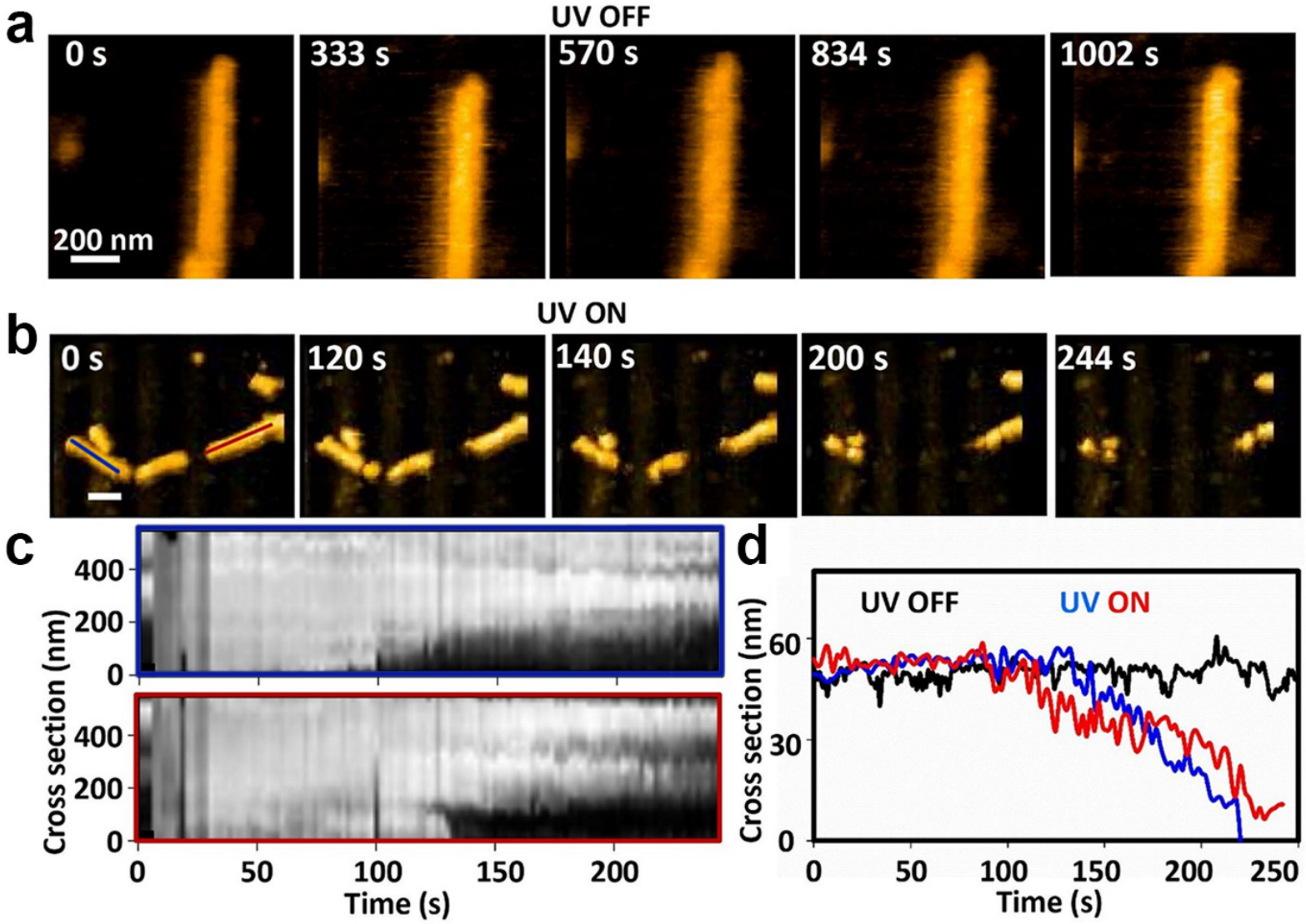
a
UV OFF
0 s
333 s
570 s
834 s
1002 s
200 nm
b
UV ON
0 s
120 s
140 s
200 s
244 s
c
Cross section (nm)
400
200
0
400
200
0
0
50
100
150
200
Time (s)
d
UV OFF
UV ON
Cross section (nm)
60
30
0
0
50
100
150
200
250
Time (s)